Inversion and Error Estimation of GPS Radio Occultation Data

Y.-H. KUO, T.-K. WEE, S. SOKOLOVSKIY, C. ROCKEN, W. SCHREINER, D. HUNT and R.A. ANTHES

University Corporation for Atmospheric Research, Boulder, Colorado, USA

Abstract

In this paper, we describe the GPS radio occultation (RO) inversion process currently used at the University Corporation for Atmospheric Research (UCAR) COSMIC (Constellation Observing System for Meteorology, Ionosphere and Climate) Data Analysis and Archive Center (CDAAC). We then evaluate the accuracy of RO refractivity soundings of the CHAMP (CHAllenging Minisatellite Payload) and SAC-C (Satellite de Aplicaciones Cientificas-C) missions processed by CDAAC software, using data primarily from the month of December 2001. Our results show that RO soundings have the highest accuracy from about 5 km to 25 km. In this region of the atmosphere, the observational errors (which include both measurement and representativeness errors) are generally in the range of 0.3% to 0.5% in refractivity. The observational errors in the tropical lower troposphere increase toward the surface, and reach ∼3% in the bottom few kilometers of the atmosphere. The RO observational errors also increase above 25 km, particularly over the higher latitudes of the winter hemisphere. These error estimates are, in general, larger than earlier theoretical predictions. The larger observational errors in the lower tropical troposphere are attributed to the complicated structure of humidity, superrefraction and receiver tracking errors. The larger errors above 25 km are related to observational noise (mainly, uncalibrated ionospheric effects) and the use of ancillary data for noise reduction through an optimization procedure. We demonstrate that RO errors above 25 km can be substantially reduced by selecting only low-noise occultations.

Our results show that RO soundings have smaller observational errors of refractivity than radiosondes when compared to analyses and short-term forecasts, even in the tropical lower troposphere. This difference is most likely related to the larger representativeness errors associated with the radiosonde, which provides in situ (point) measurements. The RO observational errors are found to be comparable with or smaller than 12-hour forecast errors of the NCEP (National Centers for Environmental Prediction) Aviation (AVN) model, except in the tropical lower troposphere below 3 km. This suggests that RO observations will improve global weather analysis and prediction. It is anticipated that with the use of an advanced signal tracking technique (open-loop tracking) in future missions, such as COSMIC, the accuracy of RO soundings can be further improved.

1. Introduction

The radio occultation (RO) technique has played an important role in characterizing planetary atmospheres since the 1960s (Kliore et al. 1964; Fjeldbo and Eshleman 1968; Lindal et al. 1983; and Lindal 1992). The planetary explorations have stimulated the theoretical study of its potential application to the Earth's atmosphere (Phinney and Anderson 1968; Lusignan et al. 1969). However, until recently RO studies of Earth's atmosphere did not receive serious consideration, primarily because of the prohibitive cost of space-borne transmitters with stable clocks and the insufficient accuracy of satellite positioning. With the realization that the Global Positioning System (GPS) could be used for occultation observa-

---

Corresponding author: Ying-Hwa Kuo, University Corporation for Atmospheric Research, P.O. Box 3000, Boulder, CO 80307, USA.
E-mail: kuo@ucar.edu.

tions, as suggested by Gurvich and Krasil'nikova (1987) and Yunck et al. (1988), application of the RO technique to the Earth's atmosphere has now become a reality (a historical survey of GPS RO sounding can be found in Yunck et al. 2000). To demonstrate the feasibility and accuracy of active atmospheric limb sounding of the Earth's atmosphere using the RO technique, UCAR established a program known as GPS/ Meteorology (GPS/MET) in May 1993, in collaboration with the Jet Propulsion Laboratory (JPL) and the University of Arizona. A proof-of-concept satellite, MicroLab-1, carrying an experimental receiver developed by JPL and Allen Osborne Associates was launched in April 1995, which marked the beginning of two years of data collection. Comparisons of GPS/MET data with models and other correlative data indicated that the GPS/MET soundings possess the equivalent temperature accuracy of ~1 K in the range from the lower troposphere to 40 km (Ware et al. 1996; Kursinski et al. 1996; Rocken et al. 1997) as well as a geopotential height accuracy of 10 to 20 m (Leroy 1997). This accuracy is comparable to that of the radiosonde system.

Following GPS/MET, two GPS RO missions were launched in 2000: the German CHAMP and the Argentinean SAC-C. These two satellites collectively produce approximately 350 RO soundings per day (Hajj et al. 2004). Both CHAMP and SAC-C are equipped with an advanced GPS occultation receiver, known as the "Black Jack," developed by JPL. This receiver is capable of tracking L2 GPS signal, modulated by Y-code, with fairly reasonable quality (above the moist troposphere), thus producing continuous RO observations (in GPS/MET this was possible during only limited periods when the Y-code was replaced by P-code). CHAMP data are used for continuous monitoring of the neutral atmosphere and study of the signals reflected from Earth's surface (Wickert et al. 2001; Beyerle et al. 2002; Wickert et al. 2004). In late 2005, the joint U.S.-Taiwan ROCSAT-3/ COSMIC mission will be launched and is expected to collect approximately 3,000 RO soundings per day. The COSMIC data will be available in near real-time and can be used to demonstrate the value of RO data for operational numerical weather prediction (NWP). In addition to COSMIC, a number of other GPS RO missions are also being developed or planned in the next ten years, including METOP, EQUARS, ACE+, and NPOESS.

The raw measurements of RO soundings are phase and amplitude of radio signals transmitted by the GPS. Based on these measurements and the knowledge of the precise positions and velocities of the GPS and low Earth orbiter (LEO) satellites, which carry GPS receivers, vertical profiles of bending angle and atmospheric refractivity are derived with the use of the local spherical symmetry assumption and Abel inversion (Phinney and Anderson 1968). Because atmospheric bending angles and refractivities (which are functions of temperature, water vapor, and pressure) are not traditional meteorological variables forecast by the models, the use of advanced data assimilation techniques, such as three-dimensional or four-dimensional variational data assimilation (3DVAR/4DVAR) systems, are required to assimilate the RO data into operational NWP systems (Eyre 1994; Kuo et al. 2000). In order to assimilate the RO data effectively, one needs to properly account for their measurement characteristics and errors. As the inversion of RO data requires various assumptions, simplifications, and approximations, the data inversion details affect the accuracy of the retrieved RO soundings and they must be taken into account in error analysis. Descriptions of end-to-end RO data processing, carried out by different research groups, can be found in Hocke (1997), Feng and Herman (1999), Steiner et al. (1999) and Hajj et al. (2002, 2004).

In preparation for the COSMIC mission, UCAR's COSMIC Data Analysis and Archive Center (CDAAC) has developed a GPS RO data processing system. The CDAAC software has been used to process GPS/MET, CHAMP and SAC-C data. In this paper, we provide a brief description of the CDAAC data processing procedures. We then evaluate the accuracy of the CHAMP and SAC-C refractivity soundings by comparing them with global analyses, global prediction, and available radiosonde observations. The primary objective of this paper is to better quantify the observational errors associated with the RO soundings. This knowledge will also help provide direction for future improvement of RO retrievals and data assimilation.

2. Inversions of GPS radio occultation data

2.1 UCAR CDAAC data processing procedures

In this section, we briefly summarize the UCAR CDAAC RO retrieval procedure. Figure 1 outlines the processing (inverting) of the RO signals, beginning with the phase and amplitude of the radio waves and precise positions and velocities of the satellites and ending with the retrieved refractivity profile at the estimated "occultation point." The various steps of the data processing can be described as follows:

Step 1: Detection of L1 tracking errors and truncation of the signal

The detection of L1 tracking errors is based on the fact that for a large enough distance from the Earth's limb to the receiver, the fractional variability of the Doppler frequency shift of the RO signal is much smaller than the corresponding variability of the refractivity in the atmosphere. This effect was first noticed and estimated by Sokolovskiy (2001b), and it makes open-loop tracking of tropospheric RO signals possible, by accurately modeling their Doppler frequency shift prior to an occultation without

a real-time correction during an occultation by use of feedback. The feedback, in closed-loop tracking, is a significant source of errors, including bias, under conditions of multipath propagation typical for the moist troposphere (Ao et al. 2003; Beyerle et al. 2003). The small variability of the atmospheric Doppler frequency shift also allows for detection of closed loop tracking errors, when their magnitude is large enough, in post-processing. For this purpose, at first, the L1 Doppler frequency shift is modeled with account for positions and velocities of the GPS and LEO and the refractivity climatology (the algorithm was introduced by Sokolovskiy 2001b). The refractivity climatology is based on CIRA+Q climate model (CIRA-86 with included moisture model below 20 km) developed by Kirchengast et al. (1999). Then the modeled Doppler is compared to the observed (smoothed) L1 Doppler. If the difference exceeds a certain threshold (which depends on LEO altitude) then the RO signal is truncated. The truncation is done at earlier time, when the difference exceeds some pre-specified fraction of the threshold. Figure 2 shows an example of L1 and L2 excess phase rates for a CHAMP occultation. Imposed is the L1 excess
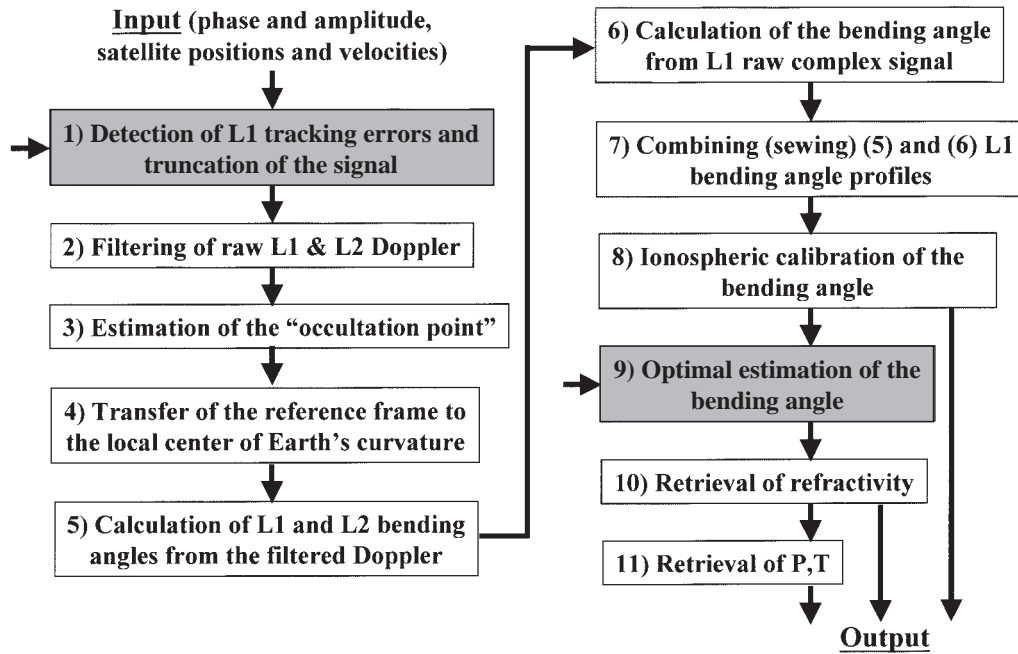

Fig. 1.   Flow diagram of the UCAR CDAAC RO data processing procedures. Arrows, incoming from sides, indicate the use of ancillary data (currently CIRA+Q).
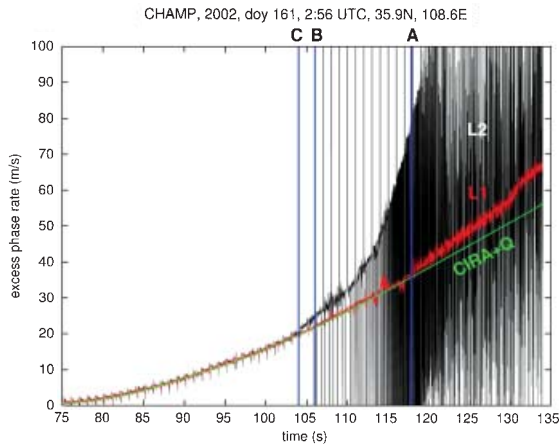
Fig. 2. Excess phase rate (Doppler) for one of CHAMP RO soundings, for L1 (red) and L2 (black) frequencies. Green line shows L1 Doppler predicted from GPS and LEO orbits and refractivity climatology (CIRA+Q). Vertical blue lines show points of the quality degradation of L1 (A) and L2 (B,C) signals below critical, as detected by automated CDAAC software (for details see text).
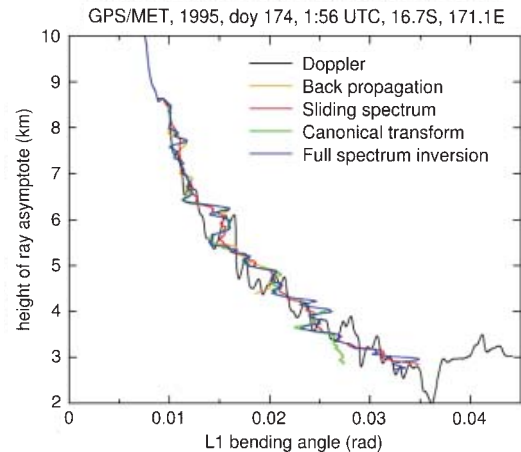

Fig. 3. L1 bending angle as a function of the height of ray asymptote derived from Doppler and from a complex signal by different radioholographic methods for one of the GPS/MET tropical occultations.

phase rate estimated from GPS and LEO orbit knowledge and CIRA+Q climatology. The beginning of an L1 tracking error (A) is detected at 117.86 s, and the RO signals at all later times are discarded.

Step 2: Filtering of raw L1 and L2 Doppler

Noise in the raw L1 and L2 Doppler signals can cause the phase of the RO signals to be taken out of the space restricted by the assumption of spherically symmetric refractivity. This, in turn, causes the bending angle, calculated from the Doppler under this assumption (see Step 5), to become a multi-valued function of the impact parameter. Such a multi-valued function cannot be inverted by the Abel technique (Step 10). Thus, the noise must be filtered out prior to the calculation of the bending angles and impact parameters. We use two methods for the low-pass filtering of phase and simultaneous calculation of Doppler: (i) cubic spline regression, and (ii) Fourier filtering with Gaussian windowing function for the spectrum. Both filters allow analytic differentiation of the phase without finite differencing and also allow the bandwidth to vary with altitude. To sup-

press the end-effects related to finite duration of a RO signal and discontinuities at ends, the RO signal is subject to extrapolation with smooth transition to a constant (zero) beyond the ends prior to Fourier filtering. Currently, we are using a constant bandwidth of 2 Hz, which, on average, provides vertical resolution consistent with the size of the Fresnel zone (~1 km) at the mean altitude of the tropopause; this is justified by reasonable agreement of Doppler and amplitude inversions (Sokolovskiy 2000). The complex RO signal, used for radioholographic inversions under conditions of multipath propagation in the troposphere, is not currently subject to any filtering.

Step 3: Estimation of the "occultation point"

The "occultation point," i.e. the point on Earth's surface to which the retrieved refractivity profile is assigned, is estimated under the tangent point of the ray connecting the GPS and LEO, with account for the ray bending, for a certain height of the ray asymptote. We define the occultation point based on the L1 excess phase = 500 m, which, on average, corresponds to 3–4 km height. The bending angle as a function of the height of the ray asymptote is estimated either from CIRA+Q refractivity climatology or from strongly smoothed L1 Doppler. At this time we use the latter approach.

Step 4: Transfer of the reference frame to the local center of Earth's curvature

As shown by Syndergaard (1998), the Earth's oblateness can introduce noticeable errors (depending on latitude) when solving the inverse problem under the assumption of spherical symmetry in the Earth-centered reference frame. In order to minimize that error (by preserving the assumption of local spherical symmetry) the center of the reference frame is transferred from the Earth's center to the virtual center of sphericity assigned to an occultation. The latter center is defined as the local center of curvature of the intersection of the Earth's reference-ellipsoid and the occultation plane (Earth's center-GPS-LEO) under the estimated "occultation point" (see Step 3).

Step 5: Calculation of L1 and L2 bending angles from the filtered Doppler

At altitudes above the moist troposphere, where multipath propagation is rare, the bending angle as a function of impact parameter of a ray is calculated from the Doppler frequency shift. The equation, which relates the Doppler frequency shift and the satellite velocities to the inclination of the phase fronts at GPS and LEO (Kursinski et al. 1997), is solved concurrently with Snell's equation (with the assumption of the spherical symmetry of refractivity) for the starting and arrival angles of the ray at the GPS and the LEO. These angles are then used to calculate both the bending angle and the impact parameter.

Step 6: Calculation of the bending angles from L1 raw complex signal

Under conditions of multipath propagation, common in the moist troposphere, the calculation of ray arrival angles from Doppler (Step 5) is not applicable. (Its formal application results in the bending angle becoming a multi-valued function of the impact parameter.) In the case of multipath propagation, the L1 bending angle is derived from the raw complex signal (phase and amplitude) by radioholographic methods, which allow disentangling of multiple tones (rays). CDAAC processing software includes four radioholographic algorithms: the back propagation (BP) method (Gorbunov and Gurvich 2000), the sliding spectral (SS) method (Sokolovskiy 2001a), the canonical transform (CT) method (Gorbunov 2002a), and the full

spectrum inversion (FSI) method (Jensen et al. 2003). The SS, CT and FSI methods all provide bending angles as a single-valued function of the impact parameter under all multipath conditions (including superrefraction). The CT and FSI methods, as shown by testing with simulated signals, provide better accuracy and resolution than the SS method. The FSI is computationally faster than the CT and currently is selected as the main inversion method in the lower troposphere. However, the data in this study were processed by using the CT method. The SS method, besides calculating the bending angles, allows visualization of the spectral content of the RO signals. The cutoff of the bending angle and refractivity profiles, retrieved by the SS, CT and FSI methods, is determined based on the fading of the amplitude of the transformed signal. Figure 3 shows a comparison of L1 bending angles derived from Doppler and from the complex signal by use of radioholographic methods. The agreement between the different radioholographic methods is substantially closer than between any of them and the Doppler method.

Recently, a heuristic method using the canonical transform applied in the sliding window (CTss) was proposed by Beyerle et al. (2004), which seems to be less sensitive to the Black Jack receiver tracking errors in the troposphere. (This comes at the expense of reduction in vertical resolution.) Also, a full spectrum inversion, applied in the sliding window of a special shape in order to suppress noise (FSIsw), has been proposed by Lohmann et al. (2003). These methods are being considered for testing in CDAAC.

Step 7: Combining (sewing) L1 bending angle profiles from Steps 5 and 6

Multipath propagation in the moist troposphere results in strong fluctuations and large tracking errors on the L2 signals, which make them unusable. A typical example is shown in Fig. 2. Large and abrupt noise increases on the L2 Doppler (B) or large mean deviation between L1 and L2 Dopplers (C), whichever occurs at the higher altitude, are used to determine the altitude $\mathbf{Z}$ below which the L2 signal is discarded for the ionospheric calibration (to be described in Step 8). The geometric optics (calculated from Doppler) L1 bending angle

(Step 5) is replaced by the radioholographic L1 bending angle (Step 6).

Step 8: Ionospheric calibration of the bending angle

The ionospheric calibration is performed by a linear combination of the L1 and L2 bending angles taken at the same impact parameter (Vorob'ev and Krasil'nikova 1994). Below the altitude where L2 is discarded (Step 7), the radioholographic L1 bending angle is corrected by the (L1–L2) bending angle extrapolated from above.

During some observation periods, CHAMP and SAC-C RO signals are contaminated by spikes in the L1 and L2 Doppler (see Section 2.3). The effect of the spikes on calibrated RO phase can be considerably reduced by applying a modified ionospheric calibration with strong smoothing of the difference of L1 and L2 excess phases on reference link (reference GPS-LEO) (J. Wickert, personal communication, 2003). While this technique almost completely suppresses the spikes in the calibrated L1 phase, for some occultations the residual effect of the spikes still remains on the L2 phases. Then the modified ionospheric correction, where the regularly smoothed L1 bending angles are corrected by strongly smoothed L1–L2 bending angles, applied for the occulted link, almost completely suppresses the effect of spikes in the ionospheric free bending angle. (A similar approach had been applied for processing GPS/MET data when L2 was subject to Anti-Spoofing.) However, this reduction of the effect of spikes, which is based on the assumption that the ionospheric effect is a smooth enough function of altitude, comes at the expense of an increase in the uncompensated ionospheric effect in the calibrated bending angle, which, for some occultations, can be larger than the effect of the spikes. These spikes are not a fundamental problem of RO, but are related to the specific hardware on CHAMP and SAC-C (see also Section 2.3).

Step 9: Optimal estimation of the bending angle

While the magnitude of the bending angle and its neutral atmosphere-related variations (signal) decrease exponentially with altitude, the magnitude of the noise (after filtering and ionospheric calibration) remains about constant

and overshadows the signal above a certain altitude (which may vary considerably between different occultations, as discussed below). To reduce the error propagation from high to low altitudes after the Abel inversion (Step 10), the observational bending angle at high altitudes must be replaced by a model (first guess) whose error is smaller than the observational noise. We use an optimal estimation of the bending angle profile prior to the Abel inversion, described by Sokolovskiy and Hunt (1996). A similar approach has been applied by Gorbunov et al. (1996), Hocke (1997), Steiner et al. (1999), Healy (2001), Gorbunov (2002b), Gobiet et al. (2002). The optimal bending angle vector $\vec{\alpha}$ (i.e., the profile $\alpha(a)$ where a is the impact parameter) is found by minimizing the cost function:

$$J(\vec{\alpha}) = (\vec{\alpha} - \vec{\alpha}_{obs})^T \hat{B}_{obs}^{-1} (\vec{\alpha} - \vec{\alpha}_{obs})$$
$$+ (\vec{\alpha} - \vec{\alpha}_{guess})^T \hat{B}_{guess}^{-1} (\vec{\alpha} - \vec{\alpha}_{guess})$$
$$= \min \qquad (1)$$

where $\vec{\alpha}_{obs}$ and $\vec{\alpha}_{guess}$ are the observational and the first guess vectors, and $\hat{B}_{obs}$ and $\hat{B}_{guess}$ are the error covariance matrices of the observations and the first guess, respectively. The solution of the linear equation $\partial J / \partial \vec{\alpha} = 0$ is:

$$\vec{\alpha}_{opt} = (\hat{B}_{obs}^{-1} + \hat{B}_{guess}^{-1})^{-1} (\hat{B}_{obs}^{-1} \vec{\alpha}_{obs} + \hat{B}_{guess}^{-1} \vec{\alpha}_{guess}) \qquad (2)$$

To simplify the solution, we arbitrarily neglect the vertical correlation in the observational noise, as well as in the error of the first guess (which results in matrices $\hat{B}_{obs}$ and $\hat{B}_{guess}$ being diagonal). Then, the optimal bending angle profile is:

$$\alpha_{opt}(a) = w_{obs}(a)\alpha_{obs}(a) + w_{guess}(a)\alpha_{guess}(a) \qquad (3)$$

where the weighting functions $w_{obs}(a)$ and $w_{guess}(a)$ are:

$$w_{obs}(a) = \frac{\sigma_{guess}^2(a)}{\sigma_{guess}^2(a) + \sigma_{obs}^2(a)} \quad \text{and}$$

$$w_{guess}(a) = \frac{\sigma_{obs}^2(a)}{\sigma_{guess}^2(a) + \sigma_{obs}^2(a)} \qquad (4)$$

On the one hand, the observational error, $\sigma_{obs}(a)$, which depends mainly on the ionospheric disturbances, varies significantly between different occultations and is estimated
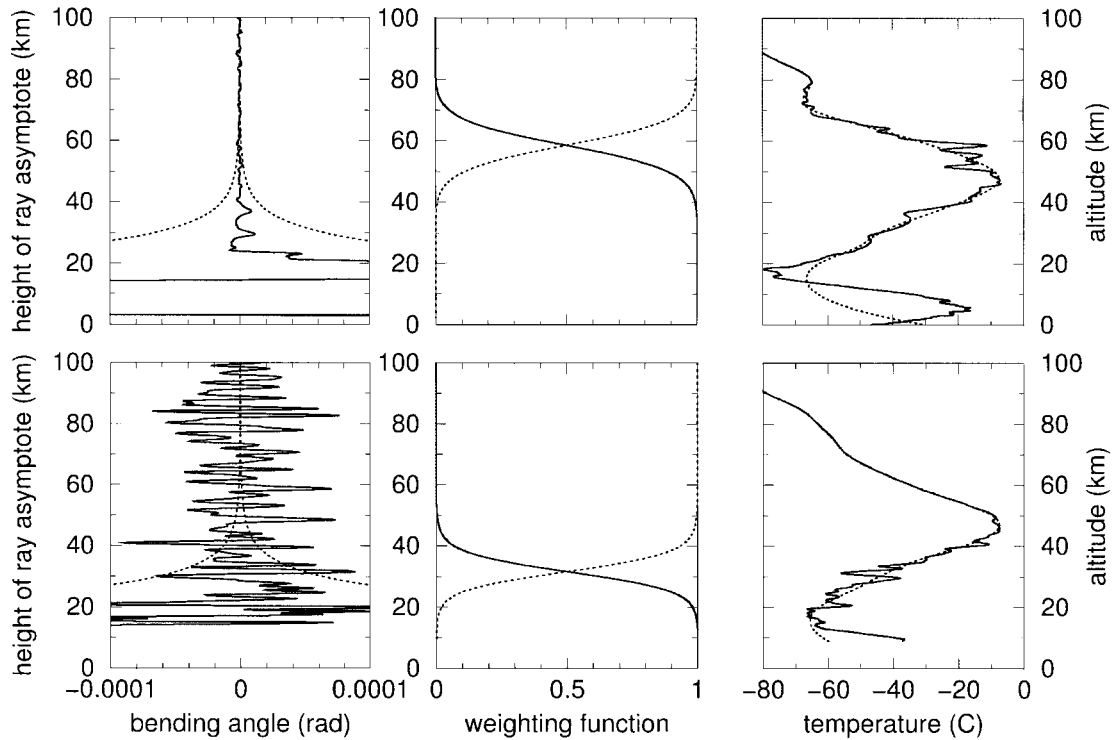
Fig. 4.   Optimization and inversion of the bending angles for two GPS/MET occultations: 1995, doy (day of year) 174, 1:56 UTC (upper panels) and 1997, doy 012, 9:58 UTC (lower panels). Left panels: deviation of the bending angle from first guess (CIRA-86) (solid line); assumed magnitude of the standard error ($\pm 20\%$) of the first guess (dotted line). Middle panels: weighting functions for the observations (solid line) and for the first guess (dotted line). Right panels: Retrieved temperatures from the optimized (weighted with the first guess) bending angle (solid line) and for the first guess (dotted line).

individually for each occultation in the altitude range of 60–80 km (where the observational noise overshadows the signal from the neutral atmosphere). On the other hand, typically, for a given occultation, the structure and the magnitude of the observational noise are rather uniform below E-layer. This allows us to consider σ_{obs} obtained at 60–80 km as an estimate for lower altitudes, i.e. to assume $\sigma_{obs}(a) = \sigma_{obs} = const$ for a given occultation. Reliable estimation of the error of the first guess, which can be represented as $\sigma_{guess}(a) = K(a)\alpha_{guess}(a)$ is more difficult. Some studies (e.g., Gorbunov 2002b) estimate K from the deviation $\alpha_{obs} - \alpha_{guess}$ in the lower stratosphere, where the effect of noise is not important, and use that K as a constant for a given occultation. However, rocket soundings have shown that the variability of density increases with altitude, and at altitudes of 30–60 km (where $w_{obs} \approx w_{guess}$ and thus the esti-

mate of K is most important for optimization) the variability can be as large as $\sim 20\%$. Currently, we define $K = 0.2$ for all occultations. Figure 4 shows $\alpha_{obs} - \alpha_{guess}$, w_{obs}, w_{guess} and the retrieved temperature profiles for two occultations with substantially different noise levels. As seen, the altitude where $w_{obs} = w_{guess}$ is different for different occultations, varying from about 30 to 60 km, depending on the observational noise σ_{obs}.

Optimization (noise reduction) of the bending angles is an underdetermined problem due to lack of information about the upper stratosphere, and different approaches discussed in the literature (see below) suffer from using different *ad hoc* assumptions. Currently, our first guess α_{guess} is based on CIRA-86. The use of a refined climatology and upper stratospheric operational numerical analysis or prediction as the first guess is under consideration. Other *ad*

hoc approaches, such as "scaling" of the first guess $c\alpha_{guess}$ and estimation of the magnitude of σ_{guess} on the basis of deviation $\alpha_{obs} - \alpha_{guess}$ at altitudes where $\sigma_{obs} \ll \sigma_{guess}$ (Gorbunov 2002b; Gobiet et al. 2002) are being considered for testing and validation.

Step 10: Retrieval of refractivity by Abel inversion

We calculate $\alpha_{guess}(a)$ and $\alpha_{opt}(a)$ in an extended vertical range by exponential extrapolation of CIRA-86 refractivity from 120 to 150 km (if an occultation starts at a lower altitude, we set $w_{obs} = 0$, $w_{guess} = 1$ above that altitude). Reconstruction of the vertical refractivity profile $N(z)$ by integration (Abel inversion) of the optimized bending angle profile $\alpha_{opt}(a)$ starts at 150 km. This basically results in retrieval of the first guess (CIRA-86) refractivity at high altitudes, $\sim$80 km. At lower altitudes the retrieved refractivity is gradually affected more by the observations, according to an increase of their weight in $\sigma_{opt}(a)$.

Step 11: Retrieval of pressure and temperature

At altitudes where humidity may be neglected (above the troposphere), pressure and temperature are reconstructed from the retrieved refractivity (which is then proportional to density) by integration of the hydrostatic equation. The integration starts at 150 km, by setting pressure and temperature to zero. This "zero initialization" does not affect the retrieved temperature at $\sim$80 km, which is close to the first guess (CIRA-86). At lower altitudes the retrieved temperatures are gradually affected by observations, according to an increase of their weight in the retrieved $N(z)$.

2.2 Quality control of inverted RO signals

Quality control (QC) of the inverted RO signals begins with the raw signals, continues in the inversion process, and ends at the inverted refractivity. Some elements of the QC were already discussed above: truncation of the L1 signal (Step 1), truncation of L2 while keeping the L1 (Step 7), and estimation of the magnitude of residual noise which controls the weighting of the observations and the first guess at high altitudes (Step 9). Overall, the quality of the retrieved bending angle and refractivity profiles is characterized in different respects by a set of parameters. The most important parameters are listed and their physical meaning is explained in Appendix A. A user can plot histograms of these parameters for a certain period in order to make a decision about using or discarding the occultations based on certain values of the parameters, thus, balancing the quality and quantity of the data for a particular study. An example of the use of a QC parameter for the selection of low-noise occultations that provide better retrieval accuracy in the upper stratosphere (at the expense of reduction in the amount of the data) is discussed in Section 3.1.

2.3 Raw data quality issues

Current missions (CHAMP and SAC-C) are experimental, and the signal tracking hardware and firmware are not yet optimized. Intensive research and development are ongoing at JPL, and considerable improvements are expected in future RO missions. Currently, both L1 and L2 signals contain receiver tracking errors and, during some periods of the missions, periodic spikes that are related to receiver clock distribution errors. The 1 s spikes in excess Doppler can be clearly seen in Fig. 2 (before March 2002, CHAMP RO signals sometimes contained 5 s spikes). The 1 s spikes make it difficult to use the affected data for study of the stratospheric gravity waves. Even though the effect of the spikes can be reduced (in a statistical sense) by applying strong smoothing of the (L1–L2) data (Section 2, Step 8), this additional smoothing can cause an increase of the retrieval errors due to uncalibrated ionospheric effect. Because of this, the spikes must be eliminated in the future. The L1 tracking errors will be eliminated by applying the open loop tracking in the lower troposphere. The largest remaining concern is the quality of the L2 signal, which may not be tracked in the open loop mode unless C/A code is available on L2.

Our analysis of SAC-C data shows that the quality of the L2 signal varied significantly from fairly good to rather poor in year 2002. Figure 5 (upper panels) shows the altitudes $\boldsymbol{Z}$, below which L2 was discarded (see Step 7 of the processing), for all processed SAC-C occultations during March and August 2002. The test for $\boldsymbol{Z}$ was started below the point where the L1 excess phase = 30 m, which approxi-
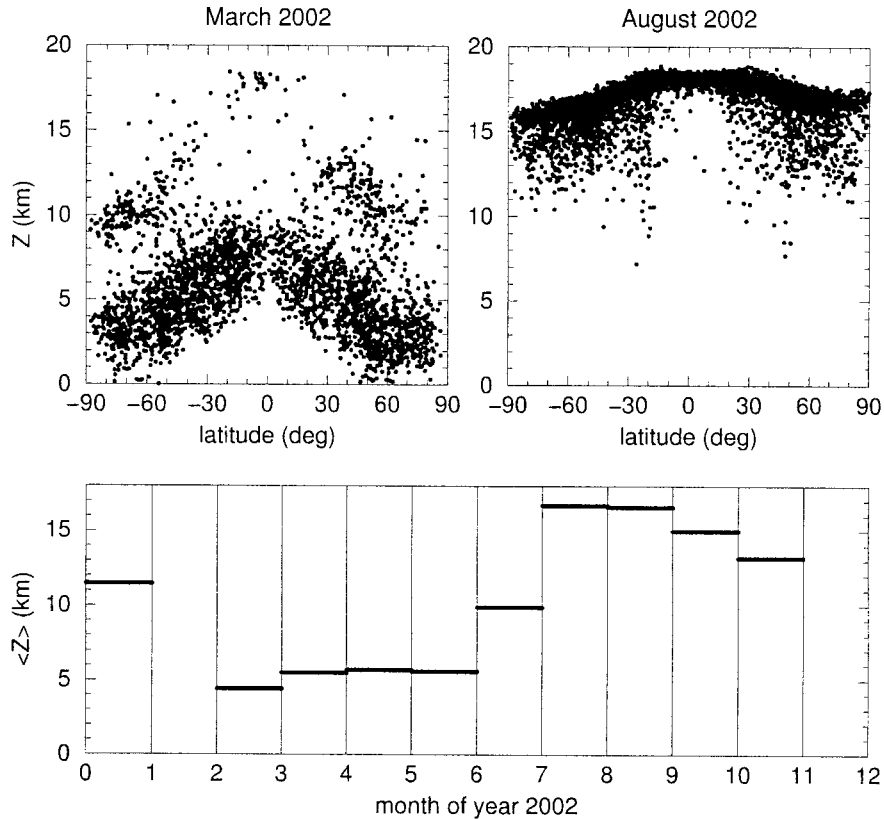
March 2002

August 2002

Fig. 5.   Upper panels: altitude **Z**, below which the L2 signal was discarded, for SAC-C, in March 2002 (fairly good L2 quality) and in August 2002 (poor L2 quality). Lower panel shows mean value of **Z** for each month of 2002.

mately corresponds to 16–18 km, depending on latitude. This starting altitude is traced by a sharp upper boundary on the scatter plot in the upper right panel of Fig. 5. It is clearly seen that L2 signals acquired by the SAC-C receiver in August 2002 are much noisier than the signals acquired in March 2002. In August 2002 there are almost no occultations with acceptable L2 quality below 10 km. The fact that the **Z** values cluster immediately below the starting altitude (upper right panel) means that for most occultations, in fact, the L2 signal has poor quality at higher altitudes. In March 2002, the **Z** values do not cluster right below the start altitude, and many occultations have acceptable L2 quality down to 5 km in the tropics and down to the surface in polar regions. Figure 5 (lower panel) shows **Z** averaged over each month in 2002 for SAC-C. The fact that the L2 signal acquisition was possible with reasonably good quality during some time periods, as can

be seen in the upper left panel of Fig. 5, indicates that the problem can be resolved by improving (correcting) receiver firmware.

3.   Analysis of CHAMP and SAC-C radio occultation soundings

3.1   Comparison of radio occultation soundings with global analyses

In this section, we evaluate the accuracy of RO data by comparing CHAMP and SAC-C RO soundings with global analyses, global forecasts and radiosonde soundings. The study is based on data for the month of December 2001. The selection of December 2001 was based on the interest in a case study to examine the impact of GPS RO data on the prediction of an intense Antarctic storm. This selection was not based on the relative quality or the quantity of the available GPS RO data. Statistically, the quality of the RO signals in the upper stratosphere and the quality of the L2 signal in the tropo-
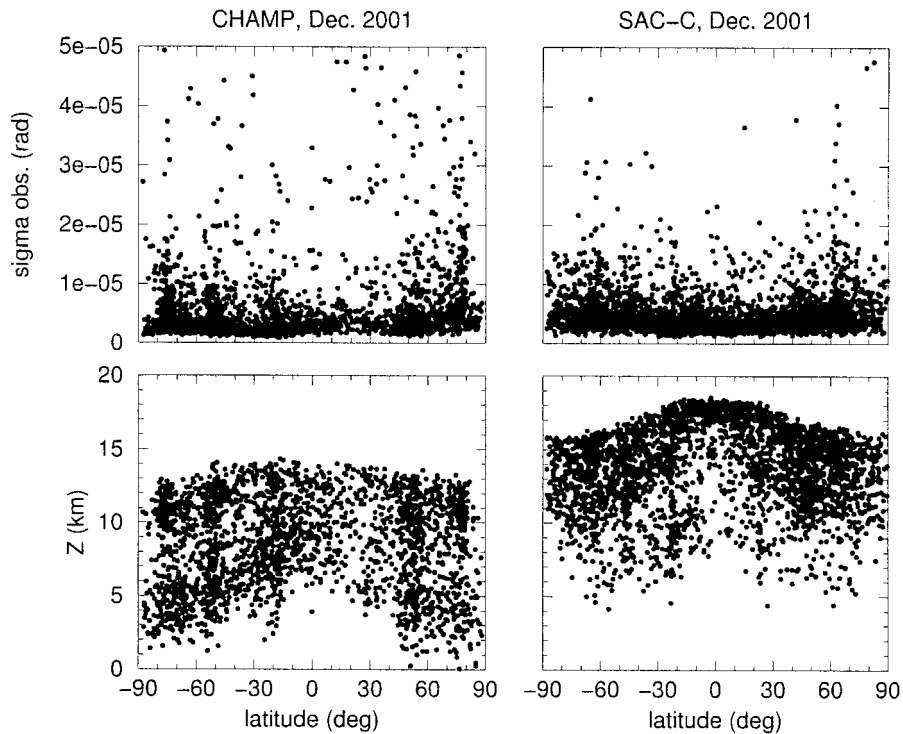
Fig. 6.   Upper panels: estimate of the observational noise of the bending angles at 60–80 km, σ_{obs}, for CHAMP and SAC-C occultations in December 2001. Lower panels: altitude $\mathbf{Z}$ below which the L2 signal was discarded.

sphere for this period are characterized by the use of two QC parameters in Fig. 6. Upper panels show the observational error σ_{obs} (standard deviation of the bending angle from first guess based on CIRA-86, estimated between 60–80 km), and lower panels show the altitude $\mathbf{Z}$ below which the L2 signal is discarded (for details see Section 2.1 and Appendix A) for each occultation in December 2001. The mean value $\langle \sigma_{obs} \rangle$ ("$\langle \ \rangle$" designates average over all the soundings for the month of December 2001) is $8.1 \cdot 10^{-6}$ rad for CHAMP, and $5.3 \cdot 10^{-6}$ rad for SAC-C. If we remove noisy soundings (with σ_{obs} exceeding $1 \cdot 10^{-5}$ rad), the monthly mean of $\langle \sigma_{obs} \rangle$ becomes $3.8 \cdot 10^{-6}$ rad for CHAMP and $4.2 \cdot 10^{-6}$ rad for SAC-C. Thus, the quality of CHAMP and SAC-C signals at high altitudes is not substantially different for the period considered, except for somewhat bigger number of outliers with large σ_{obs} for CHAMP (apparently related to signal acquisition problems, not to ionospheric effects), as can be seen from comparisons of the upper panels in Fig. 6. The quality of L2 at low altitudes, as can be seen

from the lower panels in Fig. 6, is different for CHAMP ($\langle \mathbf{Z} \rangle = 8.5$ km) and SAC-C ($\langle \mathbf{Z} \rangle = 13.8$ km). For SAC-C the L2 quality is somewhere between those for March and August 2002 (upper panels in Fig. 5). For SAC-C there are almost no occultations, while for CHAMP there are a fair number of occultations with acceptable L2 quality below 5 km. The fact that the CHAMP $\mathbf{Z}$ values do not cluster right below the start altitude for our L2 QC check (which was 13–14 km, corresponding to 40 m L1 excess phase) indicates that most occultations have reasonable L2 quality at higher altitudes.

Because of differences in vertical resolution, vertical coordinates, and horizontal smearing of RO soundings, a comparison of RO and radiosonde soundings with global analysis and other types of data is not trivial. In this study, we first exclude outliers (suspicious RO soundings from a statistical point of view) from the comparison dataset. We then perform a digital filtering to remove small-scale features with a vertical scale of less than 1 km, thus making the vertical resolution of the RO data
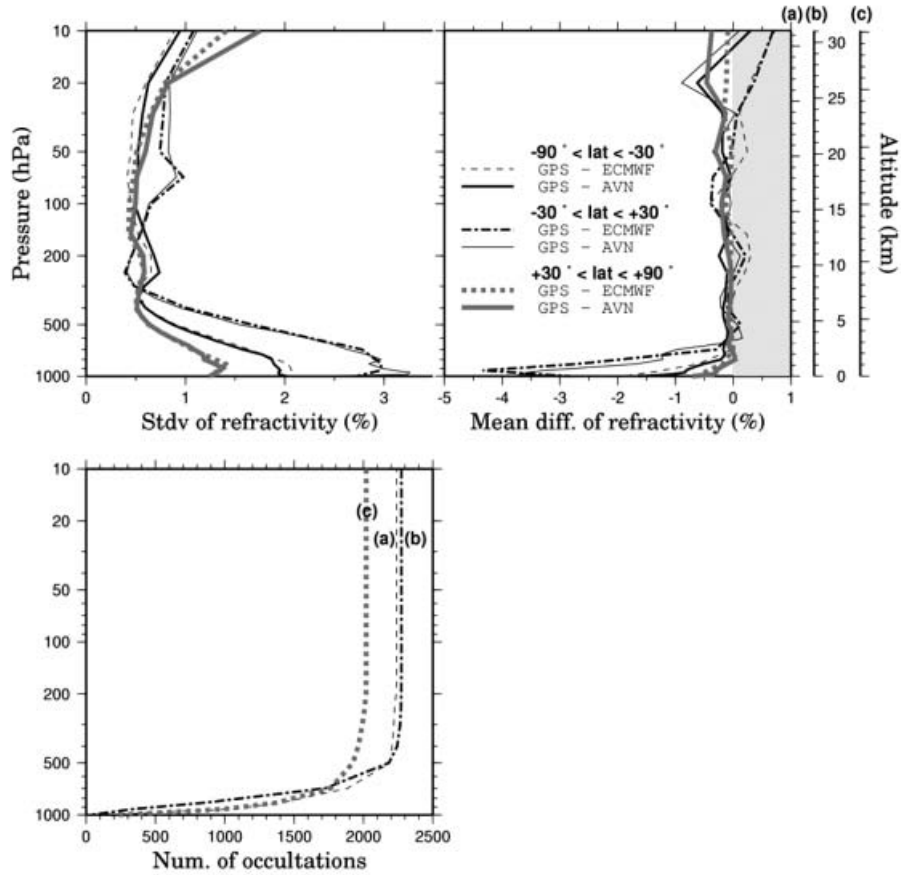
Fig. 7. Comparison of GPS radio occultation soundings with ECMWF and NCEP AVN analyses: (a) for southern hemisphere (30 S to 90 S), (b) for tropics (30 S to 30 N), and (c) for northern hemisphere (30 N to 90 N). The upper-right panel shows the mean fractional differences in refractivity, while the upper-left panel shows the standard deviations. The lower-left panel shows the total number of RO soundings used in these calculations as a function of height. The solid lines in the two upper panels are comparisons between GPS RO with NCEP AVN analysis, while the dashed lines are comparisons with ECMWF analysis. The mean altitudes corresponding to pressure surfaces are shown on right side of the upper-right panel.

compatible with other correlative data (e.g., global analyses). Finally, we compare the RO and other data on height coordinates at altitudes corresponding to constant pressure surfaces of the global analyses. Approximately 6,500 RO soundings passed the quality control procedure from the total of ∼8,500 soundings. The details of data processing and data quality control procedures are described in Appendix B. Figure 7 shows the mean and the standard deviations of fractional differences in refractivity between RO (including both CHAMP and SAC-C) and global analyses. The fractional difference in refractivity[1] ($\Delta_f N_{ij}$) between two refractivity values (N_i and N_j) is defined as the

following:

$$\Delta_f N_{ij} = \frac{N_i - N_j}{\bar{N}} \tag{5}$$

where $\bar{N}$ is the average between N_i and N_j. The refractivity values from the global analyses are local values interpolated to the time and location of the corresponding GPS occultation. The European Centre for Medium Range Weather Forecasts (ECMWF) analysis used here is the

---

1   Appendix C describes the relationship between fractional errors or differences in refractivity and the corresponding errors in temperature and water vapor pressure.

TOGA (Tropical Ocean and Global Atmosphere) analysis at 2.5 degrees horizontal resolution with 21 pressure levels. The NCEP AVN analysis is at 1 degree horizontal resolution and 26 vertical pressure levels. The comparisons are separated into three regions: northern hemisphere (30 N to 90 N), southern hemisphere (30 S to 90 S), and the tropics (30 S to 30 N).

The comparisons between the RO and ECMWF analysis and between RO and AVN analysis are very similar (Fig. 7). There are small biases between the RO soundings and the two global analyses in the bottom 2 km of the troposphere for the middle and higher latitudes. Large refractivity biases (negative N bias relative to global analyses) are found in the tropical lower troposphere, with magnitudes approaching 4% near the surface. The existence of the negative N bias was first noticed and discussed by Rocken et al. (1997) for GPS/MET, and recently confirmed by modeling receiver tracking loops (Ao et al. 2003; Beyerle et al. 2003) and superrefraction in PBL (Sokolovskiy

2003). Smaller bias (less than 1%) is found in the lowest few kilometers in middle and higher latitudes. The bias is smaller in the winter (northern) hemisphere ($\sim0.5\%$) than in the summer (southern) hemisphere ($\sim1.0\%$). This difference is presumably related to the seasonal distribution of moisture (more moisture in the summer than in the winter hemisphere). It should be noted that the significant reductions of the amount of available RO data in the lower troposphere (see lower-left panel of Fig. 7), particularly over the tropics, may affect the estimate of the bias. Noticeable bias exists in the upper stratosphere above 25 km between RO and the two global analyses. This is likely related to errors in global analyses at these altitudes as well as to RO observational (mainly residual ionospheric) errors and the errors
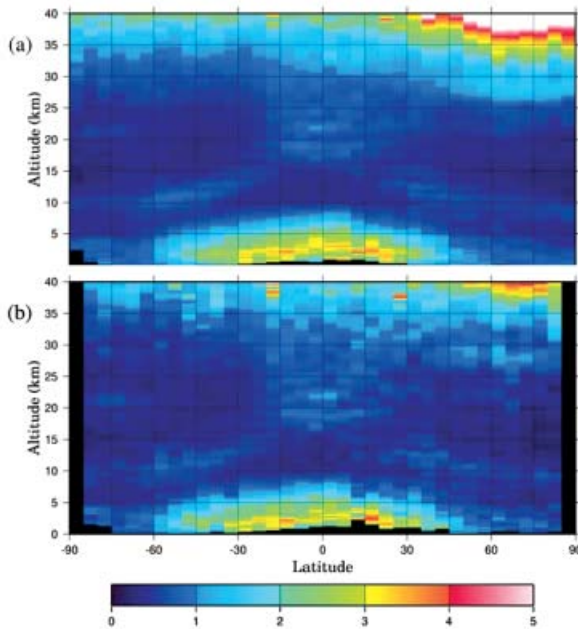

Fig. 8. (a) shows the mean standard deviations of fractional differences between RO soundings and the ECMWF global analysis for the month of December 2001. (b) is the same as (a), except the selection of RO soundings is restricted to low measurement noise (see text for details).
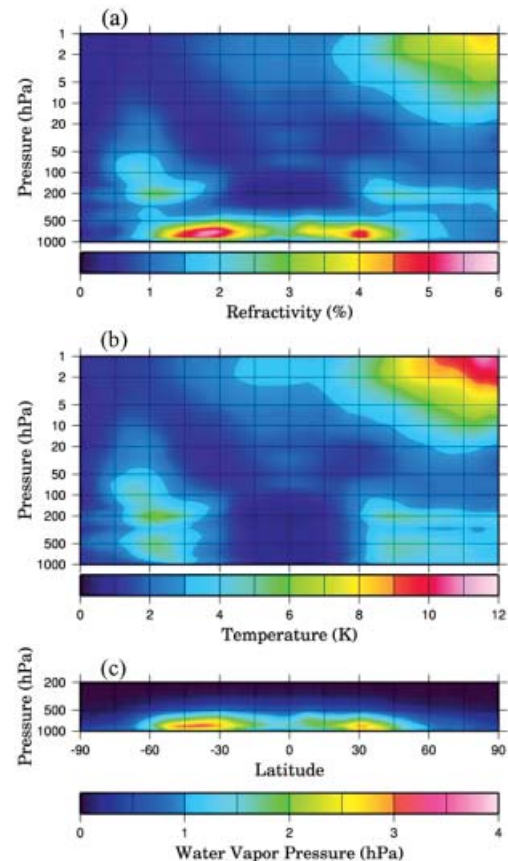

Fig. 9. The standard deviations of ECMWF analysis differences with one-day lag for December 2001: (a) refractivity, (b) temperature, and (c) water vapor pressure.

caused by the use of ancillary data for noise reduction (optimization) in RO processing.

The standard deviations (SD) of fractional refractivity differences of RO soundings from global analyses are about 0.5% between 500 hPa (~5 km) and 20 hPa (~25 km) for both hemispheres. Below 500 hPa, the SD increase to 1.3% and 2.0% for northern and southern hemispheres, respectively. In the tropics, the SD increase from about 0.5% at 300 hPa to about 3% at 1000 hPa. The SD between RO and global analyses also increase above 20 hPa, especially in the northern (winter) hemisphere.

To examine the inversion errors related to the observational noise and the use of ancillary data (e.g., CIRA climatology) for the noise reduction (optimization), we show in Fig. 8a the zonal mean SD of fractional differences in refractivity between RO and the ECMWF analysis for the month of December 2001. Two regions with large SD are found, one in the tropical lower troposphere and the other in the upper stratosphere in the northern hemisphere, from 30 N to 90 N. At 40 km, the SD between GPS and ECMWF exceed 5% (which is much larger than in the tropical lower troposphere). The upper stratosphere in winter is a region of significant variability. This follows from Fig. 9a, which presents the day-to-day refractivity variation in ECMWF analysis (e.g., the SD among one-day lagged ECMWF refractivity analyses) for December 2001. The variability in the summer stratosphere is considerably smaller. The large variability means that the daily ECMWF analysis is likely to deviate considerably from the CIRA climatology (a 40-year climatology) used as the first guess for noise reduction (optimization). Therefore, if the first guess (climatology) is weighted heavily (for a RO sounding with significant noise) in the optimized bending angle profile (as discussed in Step 9 of Section 2.1), then the resulting refractivity profile in the upper stratosphere can be subject to large errors. The weight of climatology is reduced for soundings with low noise. To demonstrate the effect of noise on inversions, we restrict the selection of RO soundings to only those with standard deviation and mean of the observed ionosphere free bending angle from the first guess at altitudes of 60–80 km to $\sigma_{obs} \leq 3 \cdot 10^{-6}$ rad and $\langle \delta\alpha \rangle \leq 5 \cdot 10^{-7}$ rad, respectively. This reduces the sample size from

6,500 to about 1,300 soundings (~20%). The result is shown in Fig. 8b. As seen, with the use of only low-noise RO soundings, the large deviation between RO and ECMWF over the winter stratosphere is mostly removed, except for the very high levels (above 37 km). This example demonstrates the clear benefit of using QC parameters, generated by the inversion software, in selecting occultations for a particular study. Thus, for climate monitoring and the study of gravity waves in the upper stratosphere, only low-noise occultations should be selected, even though this reduces the number of data. For weather prediction in the troposphere and lower stratosphere, the effects of observational noise and the use of ancillary data for noise reduction are smaller, and a larger number of occultations can be used.

Further examination of the day-to-day variability based on the ECMWF analyses shows that the variability in refractivity of the upper stratosphere in the winter hemisphere (Fig. 9a) is mainly related to the variability in the temperature field (Fig. 9b). The other high variability region in the lower troposphere from subtropical to middle latitudes, as mentioned earlier, is mainly related to tropospheric water vapor variability (Fig. 9c). A region of moderate variability in refractivity near the tropopause (at around 200 hPa near 60 latitudes of both hemispheres) is related to temperature variability associated with upper tropospheric disturbances (Fig. 9b).

Figure 10 presents a comparison between RO soundings and global analyses over land versus oceans for the northern hemisphere from 25 N to 65 N. If more than one radiosonde station is available within a 500 km radius from a given RO sounding, the location is classified as land and vice versa. For both ECMWF and AVN analyses, the results indicate that the SD between RO soundings and the global analyses are noticeably larger over oceans than over land. The accuracy of the RO soundings is expected to be about the same over ocean versus land. This suggests that the accuracy of global analyses is lower over oceans (due to the relatively smaller number of observations being assimilated). Rocken et al. (1997) arrived at a similar conclusion based on comparison of GPS/MET data to global analyses.

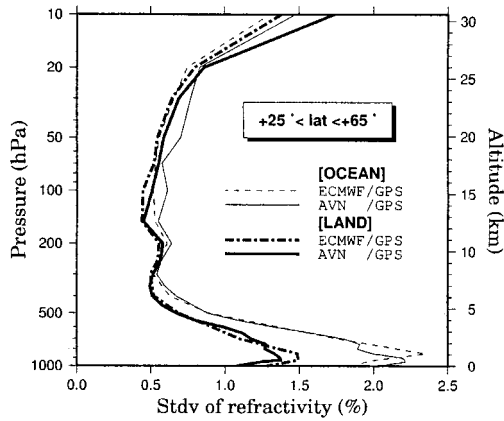Short-range (6 to 12 hours) predictions are

Fig. 10. Standard deviations of fractional differences in refractivity between RO soundings and global analyses from 25 N to 65 N. The comparisons are stratified over land versus ocean.
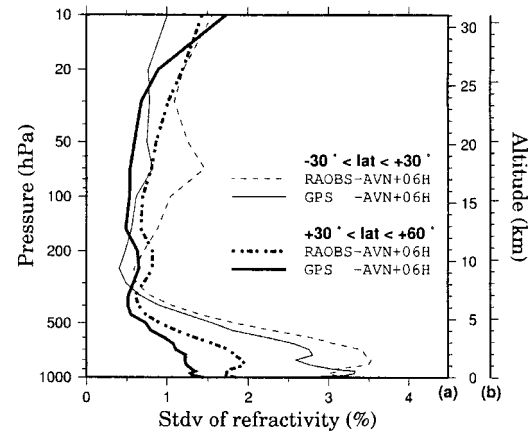

Fig. 11. Standard deviations of fractional refractivity differences between RO and NCEP AVN six-hour forecast (solid lines), and between radiosondes (RAOBS) and NCEP AVN six-hour forecast (dashed line) for December 2001. The mean altitudes corresponding to pressure surfaces are shown on the right side of the figures: (a) for the tropics (30 S to 30 N), and (b) for the northern hemisphere (30 N to 60 N).

often used as the background fields for a global analysis. Short-range predictions provide useful data sets for the evaluation of observational systems, as the forecasts are less dependent on the observations used in the analysis, the forecast errors are relatively small, and the forecast fields are more dynamically balanced than the analysis. Figure 11 compares the AVN six-hour forecast with radiosonde observations (RAOBS) and RO soundings over the tropics (from 30 S to 30 N) and over the northern hemisphere mid-latitudes (30 N to 60 N). In this comparison, only RO soundings located over land are used. Both comparisons (RO vs. forecast and radiosonde vs. forecast) are made at the time and location of each observing system. This puts RO in a slightly disadvantageous position, as additional time interpolation of the forecast fields is required for the RO vs. forecast comparison, which is not needed for the radiosonde vs. forecast comparison. We note that for both regions, RO soundings show better agreement with the AVN six-hour forecasts than the radiosonde. It is important to note that the deviation of radiosondes from the AVN forecast is larger than that of the RO observations even in the tropical lower troposphere, despite the fact that the radiosondes have smaller bias errors compared to the RO in this region of the atmosphere (figures not shown). The disagreement between radiosonde and forecast might be attributed to the mea-

surement errors of the radiosonde observing system such as inaccurate humidity measurements in the lower atmosphere (Elliott and Gaffen 1991; Schwartz and Doswell 1991; Elliott et al. 1998) and the radiation effect at higher altitudes (McMillin et al. 1992; Luers and Eskridge 1998). In addition, the radiosonde, which is a point measurement, is likely to have a larger representativeness error when compared with a global forecast. As expected, the deviations of the RO and radiosonde data from the AVN forecast are larger in the tropical lower troposphere than in the mid-latitude lower troposphere.

3.2 Estimates of GPS RO observational error and model forecast error

Short-range forecasts can be used to provide estimates of errors of an observing system. Several methods are available for this based on the statistics of observation minus forecast differences. In comparing an observing system with a short-range forecast, the difference can be considered as an apparent or perceived error. This includes the errors of the forecast as well as the observing system. Under the assumption that the observational errors are uncorrelated

with the forecast errors, the perceived error can be separated into two parts:

$$\sigma_a^2 = \sigma_b^2 + \sigma_o^2 \tag{6}$$

where σ_a^2, σ_b^2, and σ_o^2 are variances corresponding to apparent error, forecast error, and observational error, respectively. If the forecast error can be estimated accurately, then the observational error can be estimated by subtracting the forecast error variance from the total (perceived) error variance.

a. Estimation of NCEP AVN 12-hour forecast error

Two common methods are used for model forecast error estimation. The first method, known as the NMC (National Meteorological Center) method (Parrish and Derber 1992) assumes that the difference between two forecasts that are valid at the same time is a good estimate of the model forecast error. The advantage of this method is that it does not require the use of any observations to estimate model error. The weakness is that it tends to underestimate model error. The model contains only a limited spectrum of atmospheric circulations; it has greatly reduced variability compared to the true atmosphere. Moreover, the model's implicit or explicit smoothing further reduces the model variability. Finally, bias or other model errors correlated in time or between consecutive forecasts tend to cancel in the NMC method. In this study, we calculate the differences of 12-hour and 24-hour AVN forecasts for the month of December 2001 (a total of 62 pairs of forecasts).

Over the region where dense observations are available, another method proposed by Hollingsworth and Lönnberg (1986) (hereafter referred to as the H-L method) can be used to provide a more realistic estimate of model error. This method assumes that observational errors are spatially isotropic, uncorrelated with each other, and uncorrelated with forecast error. The principle of this method is to calculate a histogram of "forecast minus observation" covariances among all pairs of stations stratified against the separation distance of each pair, and then perform the least square fit of the collected correlations to an isotropic correlation model. Because any correlated error should come only from forecast fields under the given assumptions, the forecast error variance can be
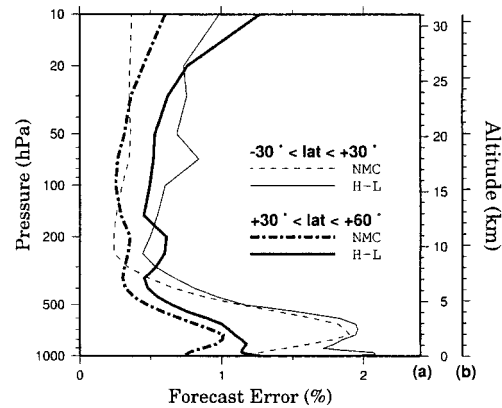

Fig. 12.   Forecast errors estimated by the NMC method (dashed line) and the Hollingsworth and Lönnberg (1986) method (solid lines). The mean altitudes corresponding to pressure surfaces are shown on the right side of the figures: (a) for the tropics (30 S to 30 N), and (b) for the northern hemisphere (30 N to 60 N).

obtained from the fitted correlation model at zero separation distance. This method is only applicable to the observational networks that are dense and large enough to provide information on diverse scales, preferably over a relatively long period of time (usually longer than a month) for a fixed set of stations. Obviously, this requirement is difficult to meet for the present study with one month of RO soundings from CHAMP and SAC-C. However, if the forecast error is assumed to be uncorrelated with the observational error, the estimated forecast error should be the same regardless of the observing system used. Therefore, our strategy is to use radiosonde observations available for the month of December 2001 to estimate the error of AVN forecasts and then to evaluate the observational error of RO soundings from the forecast error and the departure statistics of RO from the same forecast. The resulting observational error of RO is expected to be fairly reasonable, at least in the vicinity of radiosonde stations. We thus use only the RO soundings over land. The same condition has been applied for the NMC method.

The results of both methods are presented in Fig. 12. With the NMC method, the fractional refractivity error of the AVN 12-hour forecast

is very small over the tropics, above 300 hPa. The error varies from 0.3% at 300 hPa to 0.4% at 10 hPa. The AVN model error increases from 0.3% at 300 hPa to about 2% at 700 hPa. It then decreases to about 1.2% near the surface. Over the mid-latitudes (from 30 N to 60 N), the error varies from about 0.3% at 400 hPa to 0.6% at 10 hPa. The maximum error of about 1% occurs at 700 hPa.

The forecast error estimated by the H-L method is almost twice as large as those of the NMC method over the tropics above 250 hPa. The two methods produce comparable results below 500 hPa, except for the bottom 100 hPa. Near the surface, again, the H-L method gives a larger forecast error by about 0.8%. Similar results are obtained over the mid-latitudes (30 N to 60 N), with the H-L method giving a much larger estimate of forecast error than the NMC method. It is important to recognize that both the NMC and the H-L methods have short-comings; there is no perfect way to determine the true model forecast error. However, in general, the H-L method is believed to provide a more realistic estimate of the forecast error than the NMC method because actual observations are used to estimate the model forecast error.

b. Estimation of RO observational error

With the knowledge of model forecast errors, one can estimate the observational errors by subtracting the model forecast error variances from the apparent error variances. Figure 13 shows the estimates of RO observational errors based on the forecast errors obtained by the NMC method and the H-L method. Because of its larger forecast errors, the H-L method gives smaller observational errors for RO than the NMC method does. Based on the H-L method, the RO observational errors vary from about 0.2% at 400 hPa to about 0.5% at 10 hPa over the tropics. The error increases almost linearly with height (logarithm of pressure) toward the lower troposphere, from 0.2% at 400 hPa to about 3% near the surface. The RO observational errors are nearly constant at 0.3% from 500 hPa to 30 hPa over the mid-latitudes. They increase from 0.3% at 30 hPa to 1.2% at 10 hPa, and from 0.3% at 500 hPa to about 0.75% near the surface. These results show that the RO observational errors vary with latitude and altitude; thus, a single error profile is not a good global representation of the RO errors. The RO soundings have the lowest errors between the upper troposphere (~5 km) and the lower stratosphere (~25 km).
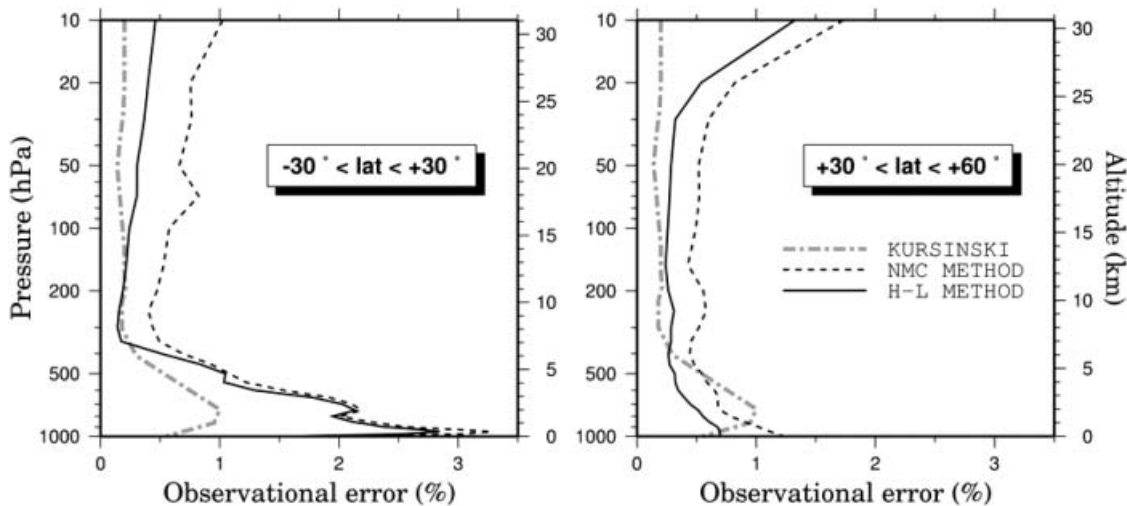

Fig. 13. RO observational errors (in terms of fractional differences in refractivity) based on the NMC method (dashed line) and the Hollingsworth and Lönnberg (1986) method (solid line). The RO measurement errors (for all latitudes) as estimated by Kursinski et al. (1997), are shown as dot-dashed lines (adapted from Fig. 13 of Kursinski et al. 1997). Left panel is for the tropics (30 S to 30 N), and the right panel is for the midlatitudes northern hemisphere (30 N to 60 N).

The RO errors, as estimated by the NMC method, are generally larger than those by the H-L method. For the tropical atmosphere above 400 hPa, and for most of the mid-latitudes troposphere and lower stratosphere, the observational errors estimated by the NMC method are about twice as large as those by the H-L method. For the tropical lower troposphere, these two methods give close results. With the more realistic estimates of model errors by the H-L method, the RO errors estimated by this method should also be more realistic.

Kursinski et al. (1997) identified a number of important sources of errors in RO measurements, and provided theoretical estimates of these errors. These errors, applicable to all latitudes, are reproduced in Fig. 13. The predicted errors are generally lower than the errors estimated in our study. For example, the maximum error predicted by Kursinski et al. (1997) in the lower troposphere is about 1%, while the error in the tropical lower troposphere estimated in our study is about 2∼3 times larger. This is to be expected, as the theoretical prediction does not take into account all the errors associated with the RO measurements (e.g., tracking errors and the effects of superrefraction in the tropical planetary boundary layer). It is important to note that for the upper troposphere and lower stratosphere, where RO is

expected to have its best performance, the measurement errors predicted by Kursinski et al. (1997) agree fairly well with the errors estimated by the H-L method (e.g., generally in the range of 0.2 to 0.3%). This suggests that the dominant error source for this region of the atmosphere is horizontal inhomogeneity along the ray path. We note that the theoretically predicted errors are larger than the estimated observational errors over the lower troposphere in the middle latitudes (30 to 60 N). In principle this can be explained by representativeness errors. Kursinski's theoretical estimates were based on comparisons with local values. In our estimates we compare the RO observations to the model refractivity, which is a horizontal average, and the difference is likely to be smaller.

Figure 14 compares the model errors with the observational errors of RO and radiosondes, based on the H-L method. It shows that RO has smaller errors than the radiosonde. This result remains unchanged using the NMC method (not shown). This is even true over the tropical lower troposphere, where the RO has the largest errors. The larger error associated with the radiosonde, which is a point measurement, is likely related to larger "representativeness" error. This is particularly true for the moisture field, which varies significantly in time and space (Fig. 9c). Another important conclusion
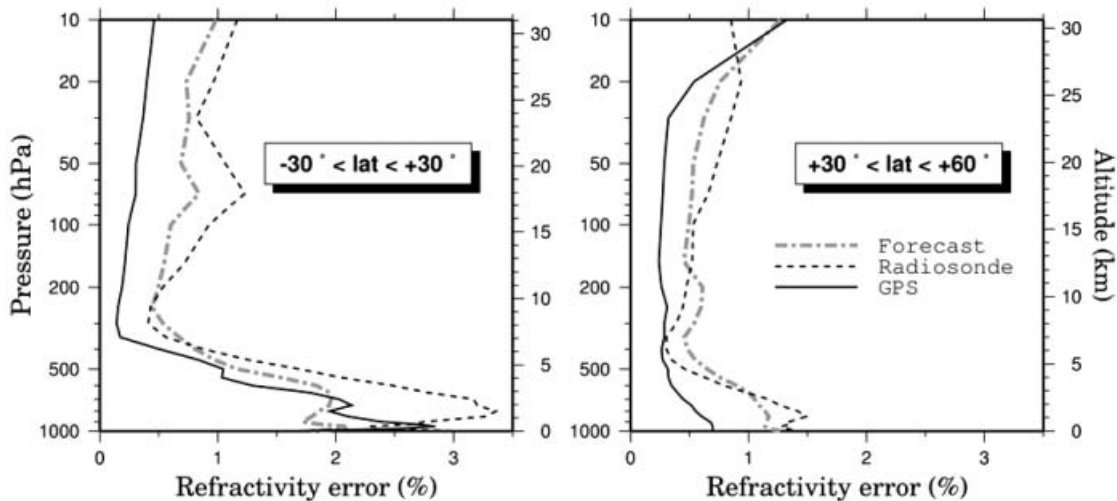

Fig. 14. NCEP AVN 12-hour forecast errors (dot-dashed lines) and observational errors of RO (solid lines) and radiosonde (dashed lines) as estimated by the Hollingsworth and Lönnberg (1986) method for the month of December 2001. Left panel is for the tropics (30 S to 30 N), and the right panel is for the midlatitudes northern hemisphere (30 N to 60 N).

is that the RO errors are significantly smaller than the AVN 12-hour forecast errors, except for the tropical lower troposphere. This indicates that the RO should contribute positively to global analysis and prediction.

3.3 Cross comparison of RO soundings

One way to assess the accuracy of the RO soundings is to compare those that took place in close proximity (Hajj et al. 2004). For the month of December 2001, we identified approximately 70 pairs of RO soundings from CHAMP and SAC-C missions that occurred within 300 km and two hours of each other. This includes CHAMP-to-CHAMP, SAC-C-to-SAC-C and CHAMP-to-SAC-C pairs. We stratify the data into three different regions: the tropics (30 S to 30 N), northern hemisphere (30 N to 90 N), and southern hemisphere (30 S to 90 S), with each region having approximately 25 pairs of soundings. The number of pairs available for comparison at a certain altitude drops significantly below 5 km and is reduced to only 5 in the lowest few kilometers. Figure 15a shows the root-mean-square (rms) of fractional differences between these RO sounding pairs. For middle and high latitudes in both hemispheres, the rms are approximately 1% between 5 km and 25 km. Above 25 km, the rms over the northern hemisphere increase to about 1.5% at 30 km.

The rms of refractivity differences (σ_G) among pairs of neighboring RO soundings (e.g., $\sigma_G^2 = \overline{(G_i - G_j)^2}$, where G_i and G_j represent a pair of RO soundings and overbar denotes the average over all collocated pairs) includes measurement errors as well as true atmospheric variability (e.g., $\sigma_T^2 = \overline{(T_i - T_j)^2}$, where T_i and T_j are the true refractivity values at the time and location of the RO soundings). One way to estimate the atmospheric variability is to repeat the same calculation using ECMWF analyzed refractivities interpolated to the RO sounding locations. The results are shown in Fig. 15b. We note that the ECMWF to ECMWF comparisons at the RO sounding sites have comparable magnitude of fractional differences as the RO to RO differences from 5 km to about 25 km for the northern and southern hemisphere. The rms increase upward from 22 km to about 30 km for the northern (winter) hemisphere, while in the southern (summer) hemisphere
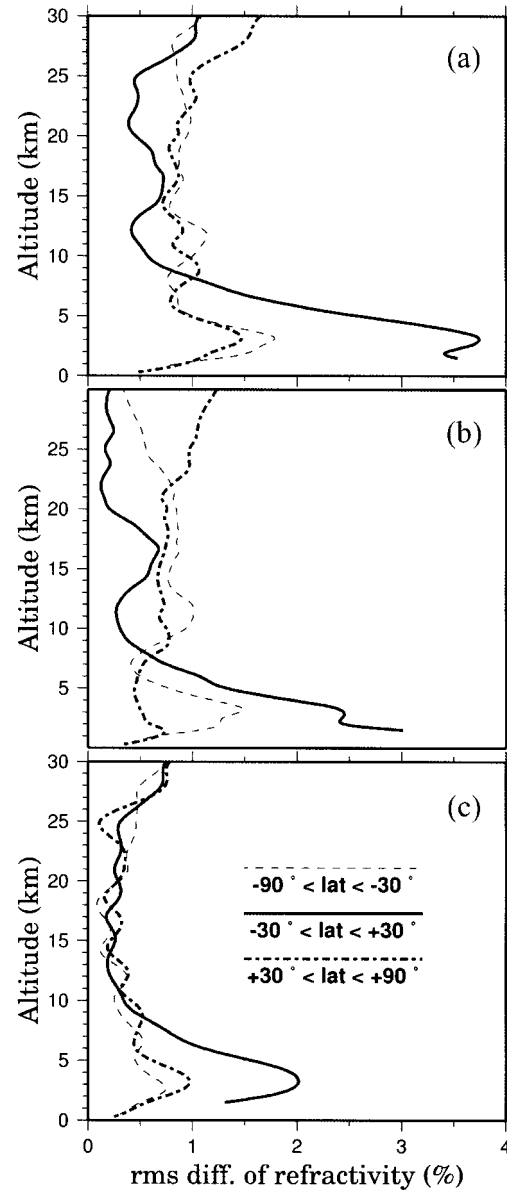

Fig. 15. (a) shows the rms of the fractional refractivity differences between pairs of RO soundings that fall within 300 km and two hours of each other. (b) is the same as (a), except for the ECMWF to ECMWF comparison at the RO sounding sites. (c) provides an estimate of the GPS measurement errors based on GPS-to-GPS comparison (see text for details).

they decrease with height. The results over the tropics yield a profile similar to that of the actual RO to RO comparisons, except the rms

are slightly smaller. The large rms at 15–18 km range are related to variability of the tropical tropopause. Above 20 km, the rms in the ECMWF simulation do not increase rapidly with height, unlike the actual RO to RO comparison. In the tropical lower troposphere, the rms of the simulated comparison increase inversely with height, and reach a value of 3% near the surface.

If we assume that the ECMWF analysis is a good approximation to the real atmosphere, then the true atmospheric variability can be approximated with the values shown in Fig. 15b: $\sigma_T^2 \approx \sigma_E^2 = \overline{(E_i - E_j)^2}$, where E_i and E_j represent the refractivity of ECMWF analysis interpolated to the RO location. Assuming measurement errors are uncorrelated with each other and uncorrelated with true atmospheric variability, the RO measurement error, σ_o can be expressed as:

$$2\sigma_o^2 = \sigma_G^2 - \sigma_T^2 \approx \sigma_G^2 - \sigma_E^2. \tag{7}$$

It is encouraging that the GPS RO measurement errors (Fig. 15c), as estimated by this approach, are similar to the observational errors estimated earlier in this section. From 5 km to 25 km, the measurement errors are generally in the range of 0.3% to 0.5% in both the northern and southern hemispheres. Over the tropics, the errors increase downward and reach a value of 2% at about 3 km. Since the number of RO to RO comparisons drops significantly below 5 km, the results below this altitude are not reliable. It is possible that the error estimates above 5 km may be larger than the true measurement errors, as the natural atmospheric variability is most likely underestimated by the ECMWF analysis, which has a horizontal resolution of 2.5 degrees and a temporal resolution of 12 hours.

4. Summary and discussions

In this paper we described the data inversion methods applied in the UCAR COSMIC Data Analysis and Archive Center (CDAAC). We then evaluated the observational errors of the RO soundings based on the data from CHAMP and SAC-C missions for the month of December 2001. Our analysis leads to the following conclusions:

(i)   The CHAMP and SAC-C RO refractivity profiles are of the highest accuracy from 5 km to 25 km. In this part of the atmosphere, there is no superrefraction, tracking errors are not very common, and the effect of the residual ionospheric noise is not significant. In this altitude range the RO refractivity errors are generally in the range of 0.3% to 0.5%. The RO measurement errors are comparable to or smaller than the 12-hour global model forecast errors. This is the region where one would expect the RO soundings to have their maximum impact on weather analysis and prediction.

(ii) The observational errors estimated from real RO soundings are, in general, larger than the theoretical predictions by Kursinski et al. (1997). In the 5-km to 25-km range, the estimated errors based on actual RO soundings are only slightly larger than the theoretical prediction. However, in the tropical lower troposphere, the estimated observational errors $(3 \sim 4\%)$ are much larger than the theoretical predictions of $\sim 1\%$. Larger observational errors are also found in the stratosphere above 25 km. These results suggest that the errors in the upper troposphere to lower stratosphere (5 km to 25 km range) are dominated by along-track horizontal inhomogeneities (Kursinski et al. 1997). Tracking errors and superrefraction (which are not considered in the theoretical estimates) contribute significantly to errors in the tropical lower troposphere. The larger errors in the upper stratosphere (above 25 km) are related to the residual ionospheric noise and the use of ancillary (climatology) data for the noise reduction process (optimization). However, the upper stratospheric errors can be substantially smaller when selecting only high quality (low noise) occultations with reduced weight of the first guess (CIRA-86 climatology) in the optimized bending angles and retrieved refractivity. This is an important result for the use of RO soundings in climate monitoring.

(iii) Observational errors compared to the analyses (which include both the measurement errors and the representativeness errors) associated with radiosondes are found to be significantly larger than those of the RO

observations. This is even true for the tropical lower troposphere. This is attributed to measurement errors of the radiosonde as well as the larger representativeness errors associated with the radiosonde, which is a point measurement.

(iv) The errors of RO soundings, as estimated by comparison of independent neighboring RO observations, are, in general, compatible with the observational errors estimated using the standard methods from 5 km to 25 km. This gives support to the estimates of the RO observational errors based on the global analyses.

The results presented in this paper indicate that the quality of RO soundings is very high in the upper troposphere and lower stratosphere. The measurement (and observational) errors in this range of the atmosphere are comparable with the theoretical predictions. However, the errors in the tropical lower troposphere and the stratosphere are considerably larger than theoretical predictions. These are the regions where further improvements in signal acquisition and sounding retrieval are most important.

Theoretically, RO remote sensing has a very high potential accuracy, which is fundamentally limited by the stability of the transmitter and receiver clocks, positioning accuracy, diffractional effects, ionospheric variability, and horizontal inhomogeneity of refractivity in the atmosphere. The horizontal inhomogeneity of the atmosphere, which makes the inverse RO problem underdetermined, requires either reduction of the dimension of the problem by using the assumption of local spherical symmetry (which introduces errors) or the inclusion of ancillary information in the inversion (variational assimilation). Superrefraction can be a significant error source below the sharp top of a marine boundary layer near 2–3 km altitude (Sokolovskiy 2003). The problem of multipath propagation, which has been previously considered as the factor restricting accuracy in the moist troposphere, has been successfully resolved by the development of advanced radio-holographic methods that allow disentangling of multiple rays. With the use of GPS, the clock stability and the positioning accuracy do not introduce a dominant error source. However, other features of GPS do not allow the potential

of the RO technique to be realized to its fullest extent. In particular, at GPS frequencies the uncalibrated ionospheric effect related to small-scale plasma irregularities is the dominant error source at altitudes above ~30 km. This effect can be significantly reduced by use of higher frequencies. Closed-loop tracking results in large errors when tracking multitone signals and is currently one of the dominant error sources in the moist troposphere. While open-loop tracking (which is free of tracking errors) can be applied for L1 (modulated by C/A code), currently it cannot be applied for L2, which is modulated by P(Y) code. The planned GPS signal modernization may solve this problem.

Acknowledgements

References

Ao, C.O., T.K. Meehan, G.A. Hajj, A.J. Mannucci, and G. Beyerle, 2003: Lower-troposphere refractivity bias in GPS occultation retrievals. *J. Geophys. Res.*, **48**, 4577, doi:10.1029/2002JD003216.

Beyerle, G., K. Hocke, J. Wickert, T. Schmidt, C. Marquardt, and C. Reigber, 2002: GPS Radio occultations with CHAMP: A radio holographic analysis of GPS signal propagation in the troposphere and surface reflections. *J. Geophys. Res.*, **107**, 4802, doi:10.1029/2001JD001402.

———, M.E. Gorbunov, and C.O. Ao, 2003: Simulation studies of GPS radio occultation measurements. *Radio Sci.*, **38**, 1084, doi:10.1029/2002RS002800.

———, J. Wickert, T. Schmidt, and C. Reigber, 2004: Atmospheric sounding by GNSS radio occultation: An analysis of the negative refractivity bias using CHAMP observations. *J. Geophys. Res.*, doi:10.1029/2003JD003922.

Elliott, W.P. and D.J. Gaffen, 1991: On the utility of radiosonde humidity archives for climate studies. *Bull. Amer. Meteor. Soc.*, **72**, 1507–1520.

———, R.J. Ross, and B. Schwartz, 1998: Effects on climate records of changes in national weather service humidity processing procedures. *J. Climate*, **11**, 2424–2436.

Eyre, J., 1994: Assimilation of Radio Occultation Measurements into a Numerical Weather Prediction System. ECMWF *Technical Memorandum No. 199*, 34 pp.

Feng, D.D. and B.M. Herman, 1999: Remotely sensing the Earth's atmosphere using the Global Positioning System. *J. Atmos. Ocean. Tech.*, **16**, 989–1002.

Fjeldbo, G. and V.R. Eshelman, 1968: The atmosphere of Mars analyzed by integrated inversion of the Mariner IV occultation data. *Planet. Space Sci.*, **16**, 1035–1059.

Gobiet, A., G. Kirchengast, U. Foelsche, A.K. Steiner, and A. Loescher, 2002: Advancements of GNSS occultation retrieval in the stratosphere for climate monitoring. *Proceedings of 2002 EU-METSAT Meteorological Satellite Data Users Conference*, 633–641.

Gorbunov, M.E., A.S. Gurvich, and L. Bengtsson, 1996: Advanced algorithms of inversion of GPS/MET satellite data and their application to reconstruction of temperature and humidity. Max-Planck Inst. For Meteor., *Tech. Rep.*, **211**, 40 pp.

——— and ———, 2000: Comparative analysis of radioholographic methods of processing radio occultation data. *Radio Sci.*, **35**, 1025–1034.

———, 2002a: Canonical transform method for processing radio occultation data in the lower troposphere. *Radio Sci.*, **37**, 1076, doi:1029/2000RS002592.

———, 2002b: Ionospheric correction and statistical optimization of radio occultation data. *Radio Sci.*, **37**, 1084, 10.1029/2000RS002370.

Gurvich, A.S. and T.G. Krasil'nikova, 1987: Navigation satellites for radio sensing of the Earth's atmosphere. *Soviet J. Remote Sensing*, **6**, 89–93 (in Russian); (1990) **6**, 1124–1131 (in English).

Hajj, G.A., E.R. Kursinski, L.J. Romans, W.I. Bertiger, and S.S. Leroy, 2002: A technical description of atmospheric sounding by GPS occultation. *J. Atmos. Solar-Terr. Phys.*, **64**, 451–469.

———, C.O. Ao, B.A. Iijima, D. Kuang, E.R. Kursinski, A.J. Mannucci, T.K. Meehan, L.J. Romans, M. de la Torre Juarez, and T. P. Yunk, 2004: CHAMP and SAC-C atmospheric results and intercomparisons, *JGR*, (submitted).

Healy, S.B., 2001: Smoothing radio occultation bending angles above 40 km. *Ann. Geophys.*, **19**, 459–468.

Hocke, K., 1997: Inversion of GPS meteorology data. *Ann. Geophys.*, **15**, 443–450.

Hollingsworth, A. and P. Lönnberg, 1986: The statistical structure of short-range forecast errors as determined from radiosonde data. Part I: The wind field. *Tellus*, **38A**, 111–136.

Jensen, A.S., M.S. Lohmann, H.-H. Benzon, and A.S. Nielsen, 2003: Full spectrum inversion of radio occultation signals. *Radio Sci.*, **38**, 1040, 10.1029/2002RS002763.

Kirchengast, G., J. Hafner, and W. Poetzi, 1999: The CIRA-86aQ_UoG model: An extension of the CIRA-86 monthly tables including humidity tables and a Fortran 95 global moist air climatology model. *Eur. Space Agency*, *IMG/UoG Techn. Rep. 8*.

Kliore, A.J., T.W. Hamilton, and D.L. Cain, 1964: *Determination of some physical properties of the atmosphere of Mars from changes in the Doppler signal of a spacecraft on an earth occultation trajectory, JPL, Technical Report* 32-674.

Kuo, Y.-H., S.V. Sokolovskiy, R.A. Anthes, and F. Vandenberghe, 2000: Assimilation of GPS radio occultation data for numerical weather prediction. *TAO*, **11**, 157–186.

Kursinski, E.R., G.A. Hajj, W.I. Bertiger, S.S. Leroy, T.K. Meehan, L.J. Romans, J.T. Schofield, D.J. McCleese, W.G. Melbourne, C.L. Thournton, T.P. Yunck, J.R. Eyre, and R.N. Nagatani, 1996: Initial results of radio occultation observations of Earth's atmosphere using the Global Positioning System. *Science*, **271**, 1107–1110.

———, ———, J.T. Schofield, R.P. Linfield, and K.R. Hardy, 1997: Observing Earth's atmosphere with radio occultation measurements using the Global Positioning System. *J. Geophys. Res.*, **102**, 23429–23465.

Leroy, S.S., 1997: Measurement of geopotential heights by GPS radio occultation. *J. Geophys. Res.*, **102**, 6971–6986.

Lindal, G.F., G.E. Wood, H. Hotz, D.N. Sweetnam, V.R. Eshleman, and G.L. Tyler, 1983: The atmosphere of Titan: An analysis of the Voyager 1 radio occultation measurements. *Icarus*, **53**, **2**, 348–363.

———, 1992: The atmosphere of Neptune: An analysis of radio occultation data acquired with Voyager. *Astron J.*, **103**, **3**, 967–982.

Lohmann, M.S., A.S. Jensen, H.-H. Benzon, and A.S. Nielsen, 2003: Radio occultation retrieval of atmospheric absorption based on FSI, *Danish Meteor. Inst.*, *Sci. Rep.* **03-01**, 38 pp.

Luers, J.K. and R.E. Eskridge, 1998: Use of radiosonde data in climate studies. *J. Climate*, **11**, 1002–1019.

Lusignan, B., G. Modrell, A. Morrison, J. Pomalaza, and S.G. Ungar, 1969: Sensing the Earth's

atmosphere with occultation satellites. *Proc. IEEE*, **4**, 458–467.

Lynch, P., 1997: The Dolph-Chebyshev window: A simple optimal filter. *Mon. Wea. Rev.*, **125**, 655–660.

McMillin, L., M. Uddstrom, and A. Coletti, 1992: A procedure for correcting radiosonde reports for radiation errors. *J. Atmos. Ocean. Tech.*, **9**, 801–811.

Parrish, D.F. and J.C. Derber, 1992: The National Meteorological Center's Spectral Statistical Interpolation analysis system. *Mon. Wea. Rev.*, **120**, 1747–1763.

Phinney, R.A. and D.L. Anderson, 1968: On the radio occultation method for studying planetary atmospheres. *J. Geophys. Res.*, **73**, 1819–1827.

Rocken, C., R. Anthes, M. Exner, D. Hunt, S. Sokolovskiy, R. Ware, M. Gorbunov, W. Schreiner, D. Feng, B. Herman, Y. Kuo, and X. Zou, 1997: Analysis and validation of GPS/MET data in the neutral atmosphere. *J. Geophys. Res.*, **102**, 29849–29866.

Schwartz, B. and C. Doswell, 1991: North American rawinsonde observations: Problems, concerns, and a call to action. *Bull. Amer. Meteor. Soc.*, **72**, 1885–1896.

Sokolovskiy, S.V. and D. Hunt, 1996: Statistical optimization approach for GPS/MET data inversions, *Proceedings of URSI GPS/MET Workshop*.

——, 2000: Inversions of radio occultation amplitude data. *Radio Sci.*, **35**, 97–105.

——, 2001a: Modeling and inverting radio occultation signals in the moist troposphere. *Radio Sci.*, **36**, 441–458.

——, 2001b: Tracking tropospheric radio occultation signals from low Earth orbit. *Radio. Sci.*, **36**, 483–498.

——, 2003: Effect of superrefraction on inversions of radio occultation signals in the lower troposphere. *Radio Sci.*, **38**, 1058, doi:10.1029/2002RS002728.

Steiner, A.K., G. Kirchengast, and H.P. Ladreiter, 1999: Inversion, error analysis and validation of GPS/MET occultation data. *Ann. Geophys.*, **17**, 122–138.

Syndergaard, S., 1998: Modeling of the effect of the Earth's oblateness on the retrieval of temperature and pressure profiles from limb sounding. *J. of Atmos. Solar-Terr. Phys.*, **60**, 171–180.

Vorob'ev, V.V. and T.G. Krasil'nikova, 1994: Estimation of the accuracy of the atmospheric refractive index recovery from Doppler shift measurements at frequencies used in the NAVSTAR system. *Atmos. Ocean. Phys.*, **29**, 602–609.

Ware, R., M. Exner, D. Feng, M. Gorbunov, K. Hardy, B. Herman, Y.-H. Kuo, T. Meehan, W.

Melbourne, C. Rocken, W. Schreiner, S. Sokolovskiy, F. Solheim, X. Zou, R.A. Anthes, S. Businger, and K. Trenberth, 1996: GPS sounding of the atmosphere: Preliminary results. *Bull. Amer. Meteor. Soc.*, **77**, 19–40.

Wickert, J., C. Reigber, G. Beyerle, R. Koenig, C. Marquardt, T. Schmidt, L. Grunwaldt, R. Galas, T.K. Meehan, W.G. Melbourne, and K. Hocke, 2001: Atmosphere sounding by GPS radio occultation: First results from CHAMP. *Geophys. Res. Lett.*, **28**, 3263–3266.

——, T. Schmidt, G. Beyerle, R. Konig, Ch. Reigber, and N. Jakowski, 2004: The radio occultation experiment aboard CHAMP: Operational data analysis and validation of vertical atmospheric profiles. *J. Meteor. Soc. Japan*, **82**, 381–395.

Yunck, T.P., G.F. Lindal, and C.-H. Liu, 1988: The role of GPS in precise Earth observation, *IEEE Position Location and Navigation Symposium (PLANS 88)*, 251–258.

——, C.-H. Liu, and R. Ware, 2000: A history of GPS sounding. *TAO*, **11**, 1–20.

Appendix A
Some parameters characterizing quality of radio occultation

$\sigma_{obs} = \sqrt{\langle (\alpha - \alpha_{guess})^2 \rangle}$: standard deviation of the observed ionosphere free bending angle from the first guess at altitudes 60–80 km (where the observational noise overshadows the signal from the neutral atmosphere for all occultations). The dominant source of noise is the uncalibrated effect of small-scale ionospheric irregularities and the magnitude σ_{obs} spans a rather large range. This parameter allows estimation of the weighting functions for the observations and for the first guess.

$\langle \delta\alpha \rangle = \langle \alpha - \alpha_{guess} \rangle$: mean deviation of the observed ionosphere free bending angle from the first guess at altitudes 60–80 km. Normally, for most occultations, $\langle \delta\alpha \rangle \ll \sigma_{obs}$. If $\langle \delta\alpha \rangle \sim \sigma_{obs}$ and σ_{obs} is much larger than its mean value; this can indicate a bias error, and such occultation must be discarded.

Z: altitude below which a low quality of L2 signal has been detected and the ionospheric calibration is performed by extrapolation of (L1–L2) from above. A large value of **Z** can indicate a low quality of L2 signal and a high probability of tracking errors at all altitudes below **Z**.

S4: normalized standard deviation of L1 signal amplitude at high altitudes. A large value

of S4 can indicate an ionospheric scintillation and a high probability of tracking errors at all altitudes.

$(\alpha_{12})_{\max}$: maximum difference of L1 and L2 bending angles above **Z**. A large value can indicate extreme ionospheric conditions or tracking errors.

$((N - N_{guess})/N_{guess})_{\max}$: maximum fractional deviation of the retrieved refractivity from the first guess.

$-(dN/dz)_{\max}$: maximum negative retrieved refractivity gradient. In the future, with elimination of L1 tracking errors by open loop tracking, this parameter can be used as the indicator of sharp tops of the moist planetary boundary layer and, potentially, superrefraction conditions (which results in a negative N bias).

Appendix B
Procedures for comparison of GPS RO data with other types of data

The comparison of RO data with other types of data is not simple because GPS occultations are sampled irregularly both in space and time. The RO sounding has much higher vertical resolution than most other correlative data (e.g., global analysis), and the latitude and longitude of the estimated perigee points of the RO change with height during an occultation (smearing effect). In this appendix, we discuss the data handling procedures for the comparison of RO data with other types of data.

1) Vertical resolution

RO has much higher vertical resolution than other satellite data, global analyses, or operational radiosonde data when reported only at standard levels. Careful attention must be paid to comparisons of RO data with data of lower resolution. In particular, one should avoid interpolation of the lower-resolution data to the levels of the higher-resolution RO data. A comparison following such an interpolation would produce small-scale features, which mainly reflect structures of the higher-resolution RO data instead of the real differences between the two. Therefore, the down sampling of RO is more reasonable in such a comparison. However, the down sampling can introduce another error—aliasing. By applying a filter, we can make the resolution of RO compatible with that of other data without introducing aliasing. This is described next.

2) Application of a filter

We first normalize the RO refractivity at each height level with a corresponding reference value (based on CIRA+Q climatology). We then interpolate the normalized refractivity profile to a dense regular height grid (at 10 m resolution). On this height grid, we remove small-scale features selectively by applying a spatial filter. The filter used in this study is a low-pass filter combined with a Dolph-Chebyshev window to prevent high-frequency oscillations (e.g., Gibbs oscillations; Lynch 1997). Since the typical vertical resolution of NWP analyses is ∼1 km, this is chosen as the cut-off length of the filter. The filter removes only the small-scale components, which have vertical scales shorter than 1 km, without affecting larger-scale structures. We then interpolate the filtered profile back to the original height levels. The filtered RO refractivity profile, which is devoid of small-scale variations, is used for comparison with other sources of data.

3) Vertical coordinate

GPS RO provides refractivity as the function of height. Consequently, it is more natural to compare RO refractivity with other types of data on height coordinates. Refractivity is a function of temperature, water vapor pressure, and pressure. The relationship is valid only for height coordinates and sometimes that tends to be a source of confusion, especially when one compares two data sets on pressure coordinates. The refractivity difference of the two data at the same pressure surface is not the same as a comparison of refractivity on the same altitude, because the height of the constant pressure surface may not be the same for these two data sets. In this study, we perform the refractivity comparison on the altitudes of the constant pressure surfaces of global analyses (models).

4) Smearing

The ray perigee point of a RO sounding varies with height, while the altitude of a constant pressure surface for a global analysis varies horizontally. For a comparison of RO with global analysis, we need to identify the intersection point between a plane of pressure level of the global analysis and the RO sounding. Since the RO sounding does not carry pressure information, this intersectional point

is not readily available. In this study, this is done through an iterative process, by searching up or down along the RO sounding while repeatedly applying horizontal interpolation to the analysis. Because the resolution of RO sounding is very high, the intersection point can be determined precisely.

5) *Removal of outliers*

As discussed earlier, RO soundings are subject to measurement errors and noise. It is feasible to remove statistically suspicious data (outliers) before comparison with global analyses. For this purpose, we first split the entire data sample (8,500 soundings over one month) into latitude bins with the size of $10°$. In each latitude bin, we calculate the fractional deviation of retrieved RO refractivity from the corresponding NWP analyses at each pressure level of these analyses. At each level, we take a GPS occultation as a sample and treat the remaining occultations as its mother group. With the particular occultation excluded, we calculate the mean value and standard deviation of the mother group. Assuming that the fractional deviations follow a Gaussian distribution, we can determine whether the sample belongs to the mother group or not. If a particular RO observation falls outside the 1% significance level, the particular sample is considered an outlier and excluded from the dataset. This procedure is repeated until no additional outliers are detected. With the recognition that observational errors of RO are vertically correlated, we reject the whole sounding if the occultation fails to pass the outlier test at any level. We perform the same outlier test using both the NCEP AVN and ECMWF analyses and accept only the occultations that pass the outlier test for both global analyses. About 6500 occultations out of 8500 original occultations passed the outlier test. The benefit of this approach is that the analysis errors and RO errors have been implicitly considered in the outlier test.

For radiosonde observations, a similar test is performed. However, a loose quality control for the parameters of temperature, dew-point temperature, and geopotential height is applied prior to the outlier test for refractivity. Assuming the radiosonde observations are vertically uncorrelated, only the particular outlier at the particular level that fails the test is removed,

and the data at other levels are kept in the data set. About 80% of radiosonde observations in volume passed the routine quality control procedure and outlier test.

Appendix C

Interpretation of refractivity differences (or errors) in terms of temperature and water vapor differences (or errors)

Fractional errors (or differences) in refractivity can be related to corresponding errors (or differences) in temperature and/or water vapor pressure for interpretation and comparison with errors from observing systems that measure temperature and water vapor directly. In general, errors in water vapor pressure contribute most to errors in refractivity in moist regions, such as the lower tropical troposphere, while temperature errors contribute most of the refractivity error in drier areas such as polar regions, upper troposphere and stratosphere. From the equation for the refractivity as a function of temperature and water vapor pressure, one can estimate the order of temperature or water vapor pressure error for a given fractional error in refractivity, assuming that the other variable is correct. Throughout most of the troposphere and stratosphere, a 1% error in refractivity corresponds to about a 2 K error in temperature (assuming no error in water vapor). Under the alternate assumption of no error in temperature, a 1% error in N corresponds to a *maximum* error of about 1 mb in water vapor pressure, and this occurs in the extremely moist tropics near the surface. The error in water vapor pressure drops off rapidly with height; for example, in a standard atmosphere the error is approximately 0.35 mb at 5 km, 0.15 mb at 10 km, and 0.03 mb at 20 km. (These numbers assume 100% relative humidity to estimate the maximum effect.)

In our study we find that errors in RO refractivity reach 3–4% near the surface in the moist tropics and average $\sim$0.3% to 0.5% over much of the rest of the troposphere and stratosphere. In the tropics, the temperature throughout the lower troposphere is fairly uniform, but the water vapor pressure shows great variability (Fig. 9c). A 3% error in refractivity corresponds to about a 3 mb error in water vapor pressure in the tropics, and it is water

vapor that contributes most to the refractivity error here. Because the saturation vapor pressure is approximately 30 mb, this error produces an error in relative humidity of about 10% in the lower tropical troposphere. In the upper troposphere and lower stratosphere where water vapor is negligible, most of the refractivity error is related to temperature; here a 0.5% error in refractivity corresponds to an error in temperature of about 1 K.